Ferromagnetic Switching of Knotted Vector Fields in Liquid Crystal Colloids

Qiaoxuan Zhang, Paul J. Ackerman, Qingkun Liu, and Ivan I. Smalyukh

Phys. Rev. Lett. **115**, 097802 — Published 28 August 2015

DOI: 10.1103/PhysRevLett.115.097802

Ferromagnetic switching of knotted vector fields

Qiaoxuan Zhang,[1,2] Paul J. Ackerman,[1,3] Qingkun Liu,[1] and Ivan I. Smalyukh[1,2,3,4,5*]

[1]Department of Physics, University of Colorado, Boulder, CO 80309, USA
[2]Materials Science and Engineering Program, University of Colorado, Boulder, CO 80309, USA
[3]Department of Electrical, Computer and Energy Engineering, University of Colorado, Boulder, CO 80309, USA
[4]Liquid Crystal Materials Research Center, University of Colorado, Boulder, CO 80309, USA
[5]Renewable and Sustainable Energy Institute, National Renewable Energy Laboratory and University of Colorado, Boulder, CO 80309, USA

*Corresponding author: ivan.smalyukh@colorado.edu

Abstract: *We experimentally realize polydomain and monodomain chiral ferromagnetic liquid crystal colloids that exhibit solitonic and knotted vector field configurations. Formed by dispersions of ferromagnetic nanoplatelets in chiral nematic liquid crystals, these colloidal ferromagnets exhibit spontaneous long-range alignment of magnetic dipole moments of individual platelets, giving rise to a continuum of magnetization field* **M**(**r**)*. Competing effects of surface confinement and chirality prompt spontaneous formation and enable optical generation of localized twisted solitonic structures with double twist tubes and torus knots of* **M**(**r**)*, which exhibit a strong sensitivity to direction of weak magnetic fields ~1 mT. Numerical modeling, implemented through free energy minimization to arrive at field-dependent three-dimensional* **M**(**r**)*, shows a good agreement with experiments and provides insights into the torus knot topology of observed field configurations and corresponding physical underpinnings.*

Envisaged by Gauss, Kelvin, and Tait, static links and knots of looped physical field lines are now experimentally realized [1-5]. Liquid crystals (LCs) permit knotting of singular linear

vortices along which molecular ordering vanishes [2,3] and also three-dimensional (3D) nonsingular topological solitons with knots and links in the molecular alignment field $\mathbf{n}(\mathbf{r})\equiv-\mathbf{n}(\mathbf{r})$, which are labeled by elements of the third homotopy group $\pi_3(RP^2)=\mathbf{Z}$ [1,4,5]. However, their $\pi_3(S^2)=\mathbf{Z}$ counterparts in vector fields, such as the magnetization field $\mathbf{M}(\mathbf{r})$, have not been experimentally realized. Such solitons are commonly unstable according to the Hobart-Derrick theorem [6], but can arise in theoretical models with higher-order spatial derivatives (Skyrme stabilization mechanism [7]). In chiral condensed matter, such as noncentrosymmetric magnets [8,9] and cholesteric LCs [1,4,5,10,11], solitons arise as mesoscopic objects due to the system's tendency of forming twisted states. For example, this enables isolated $\pi_2(S^2)=\mathbf{Z}$ solitons [12] and their condensates [13] in chiral ferromagnets with potential applications in spintronics [14], as well as isolated $\pi_2(S^2)=\mathbf{Z}$ and $\pi_3(S^2)=\mathbf{Z}$ solitons [4,11] and their self-assemblies along with other defects in chiral LCs [1,5,11].

We experimentally realize chiral ferromagnetic LC colloids (CFLCCs) with ordered ferromagnetic nanoplatelets [15] in a chiral LC host and spatially modulated, twisted $\mathbf{M}(\mathbf{r})$. Competition of medium's chirality with the strong surface anchoring at bounding substrates suppresses realization of unidirectional twist in CFLCCs and prompts spontaneous or laser-guided formation of localized twisted solitonic structures with double twist tubes and torus knots of $\mathbf{M}(\mathbf{r})$. 3D solitons exhibit a strong polar response to weak magnetic fields and are accompanied by hyperbolic point defects, forming localized field configurations dubbed "torons" [1]. Numerical free energy minimization yields 3D $\mathbf{M}(\mathbf{r})$-structures matching their experimental counterparts and reveals topologically protected particle-like configurations that resemble famous mathematical Hopf and Seifert fibrations [16].

Barium hexaferrite $BaFe_{11}CrO_{19}$ ferromagnetic nanoplatelets of thickness 10 nm and diameter 105 nm were synthesized by thermohydrodrate method [17]. They are magnetically monodomain with magnetic moments ($\approx 9 \times 10^{-18}$ Am^2) orthogonal to large-area faces. The platelets were surface-functionalized by silane-terminated polyethylene glycol (JemKem Technology) to improve stability and define homeotropic boundary conditions for **n**(**r**) in the LC. To prepare CFLCCs, 15 μL of pentylcyanobiphenyl (5CB) was mixed with 15 μL of ethanol, and then with 15 μL of 0.5-1 wt% magnetic platelet dispersion in ethanol, followed by ethanol evaporation while kept at 90 °C for 3 h. Then, the sample was rapidly cooled to the nematic phase of 5CB while vigorously stirring. The dispersion was doped with a left-handed chiral agent cholesteryl nonanoate (Sigma-Aldrich) to yield CFLCC pitch $p=1/(hC_{CN})$, distance over which **M**(**r**) ∥ **n**(**r**) in the equilibrium state rotates by 360°, where h=6.25 μm^{-1} is helical twisting power and C_{CN} is concentration of cholesteryl nonanoate. Final concentration of platelets in the LC was varied within 0.05-0.1 wt%. Nanoplatelets exhibited spontaneous alignment with large-area faces orthogonal to **n**(**r**) and magnetic moments along **n**(**r**), as confirmed by measuring polarization-dependent absorbance in planar cells (Fig. 1a) and probing response to magnetic fields. Dispersions of ferromagnetic platelets in 5CB were stable at used fields μ_0**H** up to 20 mT, exhibiting facile response to ~1 mT.

Homeotropic cells with polydomain CFLCCs, with **M**(**r**) pointing along one of the two anti-parallel directions along the vertical far-field director $\mathbf{n_0}$, were prepared using 1 or 0.17 mm thick glass plates treated with an aqueous solution of 0.1 wt% N,N-dimethyl-N-octadecyl-3-aminopropyl-trimethoxysilyl chloride (Acros Organics) to set perpendicular boundary conditions for **n**(**r**). Alternatively, polyamide SE1211 (Nissan Chemicals) alignment layers were prepared via

spin coating and baking at 185 ˚C for 1 h. To define monodomain CFLCCs with only one orientation of the far-field magnetization vector $\mathbf{M_0}$, 0.5 wt% of $BaFe_{11}CrO_{19}$ nanoplatelets were added to the polyamide and spin coated in presence of ≈40 mT field normal to the glass plate. Assuring like-orientation of easy axes for $\mathbf{M_0}$ at inner surfaces of confining plates, we defined square-inch ferromagnetic CFLCC monodomains. The cell thickness ≈60 μm was set using UV-curable optical adhesive (NOA-65, Norland Products) containing 60 μm silica spacers. The CFLCC pitch p≈70 μm was defined using C_{CN}=0.23 wt%. We probed CFLCCs (Fig. 1) using an alternating gradient magnetometer (MicroMag 2900, Princeton Measurement Corp.) and a vibrating sample magnetometer (PPMS 6000, Quantum Design). A threshold field at which magnetization reversal starts for ferromagnetic colloids in a nematic host is ≈1 mT (Fig. 1d), whereas that of CFLCC with the same concentration (0.1 wt%) of nanoparticles is ≈0.5 mT (Fig. 1b). This lower threshold for CFLCC arises due to reduction of elastic free energy of a field-distorted state with twist deformations and is similar to that in homeotropic cells of chiral LCs relative to their non-chiral counterparts [1]. Unlike non-chiral nematic dispersions of the same platelets in 5CB (Fig. 1d), which exhibit ferromagnetic response at $\mathbf{H} \parallel \mathbf{n_0}$ and paramagnetic-like response at $\mathbf{H} \perp \mathbf{n_0}$, CFLCCs with solitonic structures show hysteresis loops at both $\mathbf{H} \parallel \mathbf{n_0}$ and $\mathbf{H} \perp \mathbf{n_0}$ (Fig. 1b,c).

Laser generation of solitonic structures was done using a 100 mW, 1064 nm beam from a holographic optical tweezers setup, which was focused into a CFLCC cell by a 100× objective with numerical aperture of 1.4 [1, 18]. 3D imaging of $\mathbf{n}(\mathbf{r}) \parallel \mathbf{M}(\mathbf{r})$ utilized three-photon excitation fluorescence polarizing microscopy based on fluorescence of 5CB molecules arising from three-photon absorption of 780 nm femtosecond light, as described elsewhere [4,5]. Implemented

using an IX81 inverted microscope, this 3D imaging was utilized in combination with conventional polarizing microscopy to probe topology and switching of the solitonic structures.

CFLCC cells with vertical surface boundary conditions for $\mathbf{n_0}$ without selection of one of the two anti-parallel $\mathbf{M} \parallel \mathbf{n_0}$ orientations are polydomain in nature (Fig. 2a-f), with regions of opposite **M** separated by wall defects "invisible" before (Fig. 2a) and apparent after applying fields (Fig. 2c-f). Lateral dimensions of these domains are 2-10 times cell thickness. In monodomain samples (Fig. 2g,h), magnetization alignment layers define the same $\mathbf{M_0}$ within an inch-wide cell, showing no response to $\mathbf{H} \parallel \mathbf{M_0}$ and facile spatially uniform switching at other **H** orientations, including anti-parallel to $\mathbf{M_0}$. Similar to chiral LCs without dispersed platelets [1,4,5,11,19], CFLCCs can host laser-generated or naturally occurring solitonic structures, which in polydomain samples can be embedded within single or multiple domains. Since such solitons are ~1000 times larger than nanoplatelets, mechanical coupling through surface boundary conditions forces platelets to orient orthogonally to **n**(**r**) and their magnetic dipoles along **n**(**r**) (inset of Fig. 1a) [15], so that the spatially varying **M**(**r**) is continuous and follows the director everywhere.

Consistent with 3D nonlinear optical imaging of **n**(**r**), similar to that reported elsewhere [4,5], numerical models of $\mathbf{M}(\mathbf{r}) \parallel \mathbf{n}(\mathbf{r})$ reveal torons with knotted solitonic **M**(**r**) accompanied by point defects (Fig. 3). A mid-plane cross-section of the 3D solitonic structure shows a 2π twist of **M**(**r**) in all radial directions (Fig. 3a). By numerically following **M**(**r**) field lines from a representative set of points of this cross-sectional plane [21], corresponding to a circle marked on S^2 in the inset of Fig. 3d, we find that **M**(**r**) forms closed loops, all of which are linked with each other once and define a torus (Fig. 3b), like in the mathematical Hopf fibration and field

configurations of “hopfions” [4,5]. At confining surfaces, two hyperbolic torons in defects, similar to the ones in **n**(**r**) of chiral nematics [1], match **M**(**r**) of toron’s interior with the anti-parallel to it $\mathbf{M_0}$ (Fig. 3d).

CFLCC solitons exhibit a facile orientation-dependent response to magnetic fields (Figs. 4 and 5), consistent with presence of the term $-\mu_0 \int (\mathbf{M} \cdot \mathbf{H}) dV$ in the free energy functional [15,21]. In both monodomain and polydomain samples, lateral dimensions of 3D topological solitons increase when **H** is along the vertical **M**(**r**) in the toron center and anti-parallel to **M**(**r**) around its exterior (Fig. 4a,b). Torons in monodomain CFLCCs (Fig. 4d) and the ones embedded in large domains of polydomain samples shrink when **H** is reversed, until eventually disappearing (Fig. 4e,f). However, some torons in polydomain CFLCCs exhibit a more complex behavior for **H** anti-parallel to **M**(**r**) in their interior (Fig. 4c), shrinking in size for some time and then laterally shifting to a near-by domain of opposite background magnetization and expanding similar to torons in domains with **H** along the vertical **M**(**r**) in the toron center [21]. This relatively slow response is present well below the threshold for realignment of monodmain CFLCCs with $\mathbf{M}_0$ anti-parallel to **H** in similar cells (Fig. 1), which is because of the distorted **M**(**r**) (Fig. 4). Upon turning **H** off, expanded or contracted torons relax to their initial size (Fig. 4a-d), unless **H** anti-parallel to **M**(**r**) in the toron interior exceeded a certain critical value (dependent on nanoplatelet concentration), at which the shrinking torons abruptly and irreversibly disappear. Lateral size of torons cannot shrink below ≈50% of its equilibrium value at **H**=0, at which a discontinuous re-configuration of **M**(**r**) (Fig. 4e,f) from the initial knotted/linked to a uniform field state occurs. This type of switching is a salient feature of topology-protected torus knot of **M**(**r**) within the toron (Fig. 3).

Our translationally invariant CFLCC solitons resemble both cholesteric fingers of the second kind [11,19] and 2D skyrmions in epitaxial MnSi thin films [20] (Fig. 5a,b). The soliton contains a double twist tube accompanied by a nonsingular bimeron-like structure [20] (Fig. 5a). Projection of **M**(**r**) from this cross-section onto the order parameter space, an S^2-sphere, covers it once (Fig. 5b). Switching of 2D solitons is also orientation-dependent (Fig. 5c-e). Their double-twist-tube expands when **H** matches **M**(**r**) along its axis but shrinks in the anti-parallel case, causing corresponding changes of the overall width of solitons (Fig. 5). This behavior is natural as the free energy is minimized in respective cases, consistent with the outcomes of numerical modeling (Fig. 5c,d) [21] as the field prompts expansion of CFLCC regions with **M**(**r**) $\parallel$ **H** and shrinking of regions with **M**(**r**) anti-parallel to **H**.

The observation of magnetic hysteresis curves at $\mathbf{H}\perp\mathbf{n_0}$ (Fig. 1c) is due to the localized soliton interior regions having **M**(**r**) $\parallel$ **n**(**r**) orthogonal to $\mathbf{M_0}$. Beyond these solitons, which are stabilized by the chiral nature of CFLCCs and the ensuing non-trivial topology [1,5] and can exist at no fields, many long-lived metastable spatial patterns of **M**(**r**) emerge in the confinement-frustrated CFLCCs as a result of magnetic switching, including periodic stripe patterns (supplementary Fig. S2) [21] that can persist for hours after the field is turned off. This behavior may be related the natural tendency of soft matter systems with polar ordering to realize splayed physical fields like **M**(**r**) and can be used in realizing other solitonic configurations, showing a need of developing theoretical foundations for CFLCCs beyond the simple model adopted here [15,21]. These theories may build on studies of solitons in related condensed matter systems of chiral LCs and ferromagnets [1,4,5,7-10], including modeling of 3D ferromagnetic hopfions [22], albeit CFLCCs differ from both and may enrich our understanding

of multidimensional solitons. It will be of interest to probe how the topological Hopf index of 3D solitons can be controlled when they are laser-generated standalone or along with other defects. CFLCCs may also become a model system for understanding hopfions beyond condensed matter in physical systems ranging from elementary particles to Bose-Einstein condensates and cosmology, in which physical underpinning of anticipated stabilization of 3D solitons are typically different, but experimental tests of theories are limited [23-31].

To conclude, we have experimentally realized and numerically modeled 2D skyrmionic and 3D knotted magnetization vector field configurations in a novel soft matter system of CFLCCs. We have demonstrated ferromagnetic switching of such solitons. Although knotted static solitons have been recently controllably and abundantly generated in frustrated chiral LCs in a non-polar director line field [1,4,5], the knotted configurations demonstrated here are the first such experimental realizations for the magnetization vector field. This work may be extended to obtaining isolated 3D magnetization solitons of different Hopf index and their assemblies into lattices with and without other defects [5]. The experimental platform we have developed may allow for probing topological transformation of solitonic field configurations driven by weak external stimuli, with potential uses ranging from modeling similar phenomena in other branches of physics, such as particle physics and cosmology [23-31], to applications in magneto-optic devices [32, 33].

Figure Captions:

FIG. 1. Characterization of CFLCCs. (a) Optical absorbance at light polarizations $\mathbf{P} \parallel \mathbf{n_0}$ and $\mathbf{P} \perp \mathbf{n_0}$ for a 60 μm thick planar cell with ferromagnetic platelets at 1.6 wt% in 5CB, as schematically

shown in the inset. (b-c) Magnetic hysteresis loops for the monodomain CFLCC containing solitonic structures with (b) $\mathbf{H} \parallel \mathbf{n_0}$ and (c) $\mathbf{H} \perp \mathbf{n_0}$. (d) Similar data for a monodomain non-chiral ferromagnetic platelet dispersion in 5CB. The concentration of platelets in (b-d) is ≈0.1 wt%.

FIG. 2. Polydomain and monodomain confined CFLCCs with p≈70 μm in homeotropic cells of thickness ≈60 μm. (a) A polarizing optical micrograph of a polydomain cell at no fields shown schematically in (b). (c-f) Polarizing micrographs of the same cell area for (c,d) vertical and (e,f) in-plane **H**. (g,h) Polarizing optical micrographs of a monodomain CFLCC (g) at no fields (remains unchanged for $\mathbf{H} \parallel \mathbf{M_0}$) and (h) at **H** along the arrow. The insert in (g) schematically shows a single magnetic domain of the cell. The field is ≈6 mT and platelet concentration is ≈0.05 wt%.

FIG. 3. CFLCC toron with a torus knot field configuration. (a) An in-plane cross-section of a toron passing through the cell midplane, with colors and arrows showing **M**(**r**)-orientations. (b) A torus formed by a dense series of inter-linked closed loops of **M**(**r**) intersecting the cross-section (a) in regions of the same **M**(**r**)-orientation and color; two of these loops are decorated by arrows. **M**(**r**) along the central straight and circular axes of the double twist torus are shown in blue and red, respectively, corresponding to colors in (a). (c). A vertical cross-section of the toron along a horizontal line in (a), with black circles marking hyperbolic point defects. (d) Hopf fibration representing topology of **M**(**r**) in the central part of the CFLCC toron, with the color of fibers corresponding to points on S^2 (inset) and correlated to that of **M**(**r**) in (a,b).

FIG. 4. Ferromagnetic switching of torons. (a, b) Relative lateral toron area A/A_0 vs. time in (a) polydomain and (b) monodomain CFLCCs for **H** along **M**(**r**) in the toron center, obtained experimentally. Insets in (a) show corresponding polarizing micrographs; the white scale bar in the top-left inset is 50 μm. (c,d) A/A_0 vs. time for **H** anti-parallel to **M**(**r**) in the toron center and parallel to that of its exterior for (c) polydomain and (d) monodomain samples. **H** is turned on and off at times indicated by arrows in (b,d). In a polydomain cell (c), at a constant **H**, the toron first shrinks and then expands while laterally shifting (along the white arrow in the bottom-right insert) to self-embed in a domain with a background **M** opposite to that of original domain. (e,f) A/A_0 vs. $|\mathbf{H}|$ for two opposite vertical field orientations in (e) polydomain and (f) monodomain CFLCCs. **H** is along and anti-parallel to **M**(**r**) in the toron center for $A>A_0$ and $A<A_0$, respectively. Concentrations of magnetic particles in both cases are ≈0.05 wt%.

FIG. 5. Ferromagnetic switching of 2D solitons. (a) A translationally invariant solitonic **M**(**r**) shown using arrows. (b) The corresponding S^2 order parameter space, with colors depicting vector orientations correlated with (a); the circle corresponds to the continuous **M**(**r**)-rotation along the black line in (a). (c) Experimental relative change of diameter d/d_0 of a double-twist-tube vs. time at different **H** along **M**(**r**) on tube axis (positive H marked on the plot) and at **H** anti-parallel to **M**(**r**) on tube axis (negative H). (d) Relative change of the overall width w/w_0 of the translationally invariant 2D soliton and diameter d/d_0 of the double-twist-tube within it vs. $|\mathbf{H}|$. **H** along and anti-parallel to **M**(**r**) on the double-twist tube axis yields $w>w_0$ (and $d>d_0$) and $w<w_0$ (and $d<d_0$), respectively. Numerical simulations of **M**(**r**) are calibrated using experiments. (e) Computer-simulated cross-sections of the 2D soliton at no fields (left) and for **H** pointing into the screen (middle) and out of the screen (right). Concentration of platelets is ≈0.05 wt%.

References

1. I. I. Smalyukh, Y. Lansac, N. A. Clark, R. P. Trivedi. *Nature Mater.* **9**, 139-145 (2010).
2. U. Tkalec, M. Ravnik, S. Čopar, S. Žumer, I. Muševič. *Science* ***333***, 62-65 (2011).
3. A. Martinez, M. Ravnik, B. Lucero, R. Visvanathan, S. Žumer, I. I. Smalyukh. *Nature Mater.* ***13***, 258-263 (2014).
4. B. G. Chen, P. J. Ackerman, G. P. Alexander, R. D. Kamien, I. I. Smalyukh. *Phys. Rev. Lett.* **110**, 237801 (2013).
5. P. J. Ackerman, J. van de Lagemaat, I. I. Smalyukh. *Nature Comm.* **6**, 6012 (2015).
6. G.H. Derrick. *J. Mathematical Phys.* **5**, 1252–1254 (1964).
7. T.H.R. Skyrme. *Proc. R. Soc. Lond. A* **260**, 127 (1961)
8. M.N. Wilson, A. Butenko, A.N. Bogdanov, T.L. Monchesky. *Phys Rev B* **89**, 094411 (2014).
9. A. Bogdanov, A. Hubert. *JMMM* **138**, 255-269 (1994);
10. A. O. Leonov, I. E. Dragunov, U. K. Roßler, A. N. Bogdanov, *Phys Rev E* **90**, 042502 (2014).
11. P. J. Ackerman, R. P. Trivedi, B. Senyuk, J. van de Lagemaat, I. I. Smalyukh. *Phys. Rev. E* **90**, 012505 (2014).
12. N. Romming, C. Hanneken, M. Menzel, J. E. Bickel, B. Wolter, K. von Bergmann, A. Kubetzka, R. Wiesendanger. *Science* **341***,* 636-639 (2013).
13. X. Z. Yu, Y. Onose, N. Kanazawa, J. H. Park, J. H. Han, Y. Matsui, N. Nagaosa, Y. Tokura. *Nature* **465**, 901-904 (2010).
14. A. Fert, V. Cros, J. Sampaio. *Nature Nanotech* **8**, 152-156 (2013).
15. A. Mertelj, D. Lisjak, M. Drofenik, and M. Čopič. *Nature* ***504***, 237-241 (2013).
16. H. Hopf. *Selecta Heinz Hopf* (Springer Berlin Heidelberg, German, 1964).
17. D. Lisjak and M. Drofenik. *Cryst. Growth Des.* **12**, 5174-5179 (2012)
18. R. P. Trivedi, D. Engstrom, I. I. Smalyukh. *J. of Optics* **13**, 044001 (2011).
19. P. Oswald, J. Baudry, and S. Pirkl. *Phys. Rep.* **337**, 67-96 (2000).
20. M. N. Wilson, E. A. Karhu, A. S. Quigley, U. K. Roßler, A. B. Butenko, A. N. Bogdanov, M. D. Robertson, and T. L. Monchesky. *Phys Rev B* **86**, 144420 (2012).
21. See Supplemental Material for details of numerical modeling and relaxation kinetics of stripe patterns in **M**(**r**).
22. A.B. Borisov, F.N. Rybakov. *Low Temp. Phys.* **36**, 766-771 (2010).
23. A. F. Ronada, J. L. Trueba. *Nature* **383**, 32 (1996).
24. Y. Kawaguch, M. Nitta, M. Ueda. *Phys. Rev. Lett.* **100**, 180403 (2008).
25. Y. K. Liu, C. Zhang, S. J. Yang. *Phys. Lett. A* **377**, 3300-3303 (2013).
26. N. R. Cooper. *Phys. Rev. Lett.* **82**, 1554-1557 (1999).
27. P. Sutcliffe. *Phys. Rev. B* **76**, 184439 (2007).
28. S. Bolognesi, M. Shifman, Phys. Rev. D 75, 065020 (2007).
29. A. Gorsky, M. Shifman, A. Yung. Phys. Rev. D 88, 045026 (2013).
30. A. Acusa, E. Norvaišasa, Ya. Shnir. *Phys. Lett. B* **733**, 15–20 (2014).
31. A. Thompson, A. Wickes, J. Swearngin, D. Bouwmeester. *J. Phys. A* **48**, 205202 (2015).
32. A. Mertelj, N. Osterman, D. Lisjak and M. Čopič. *Soft Matter* **10**, 9065-9072 (2014).
33. A. J. Hess, Q. Liu and I. I. Smalyukh. *Appl. Phys. Lett.* Accepted (2015).

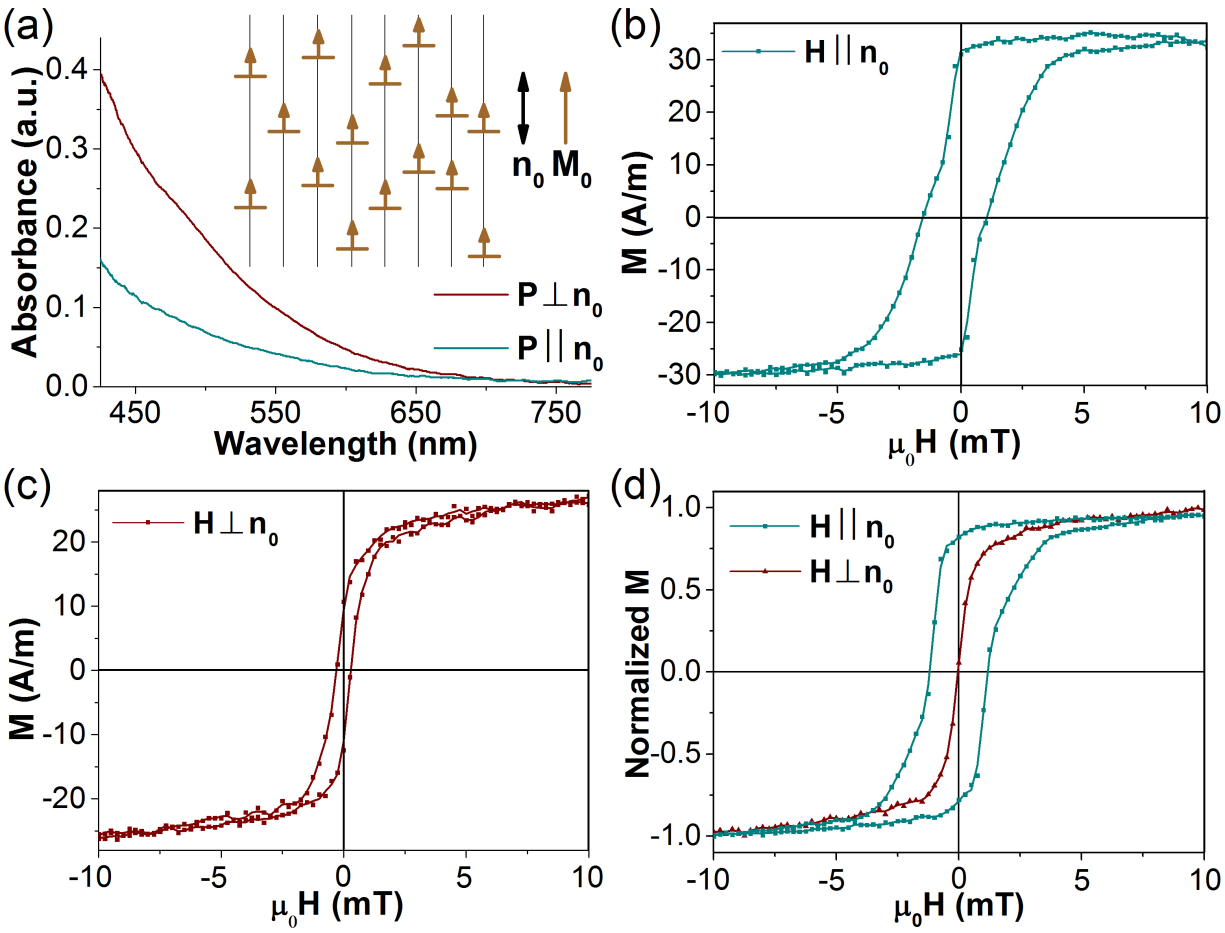

Figure 1 LE15437 04AUG2015

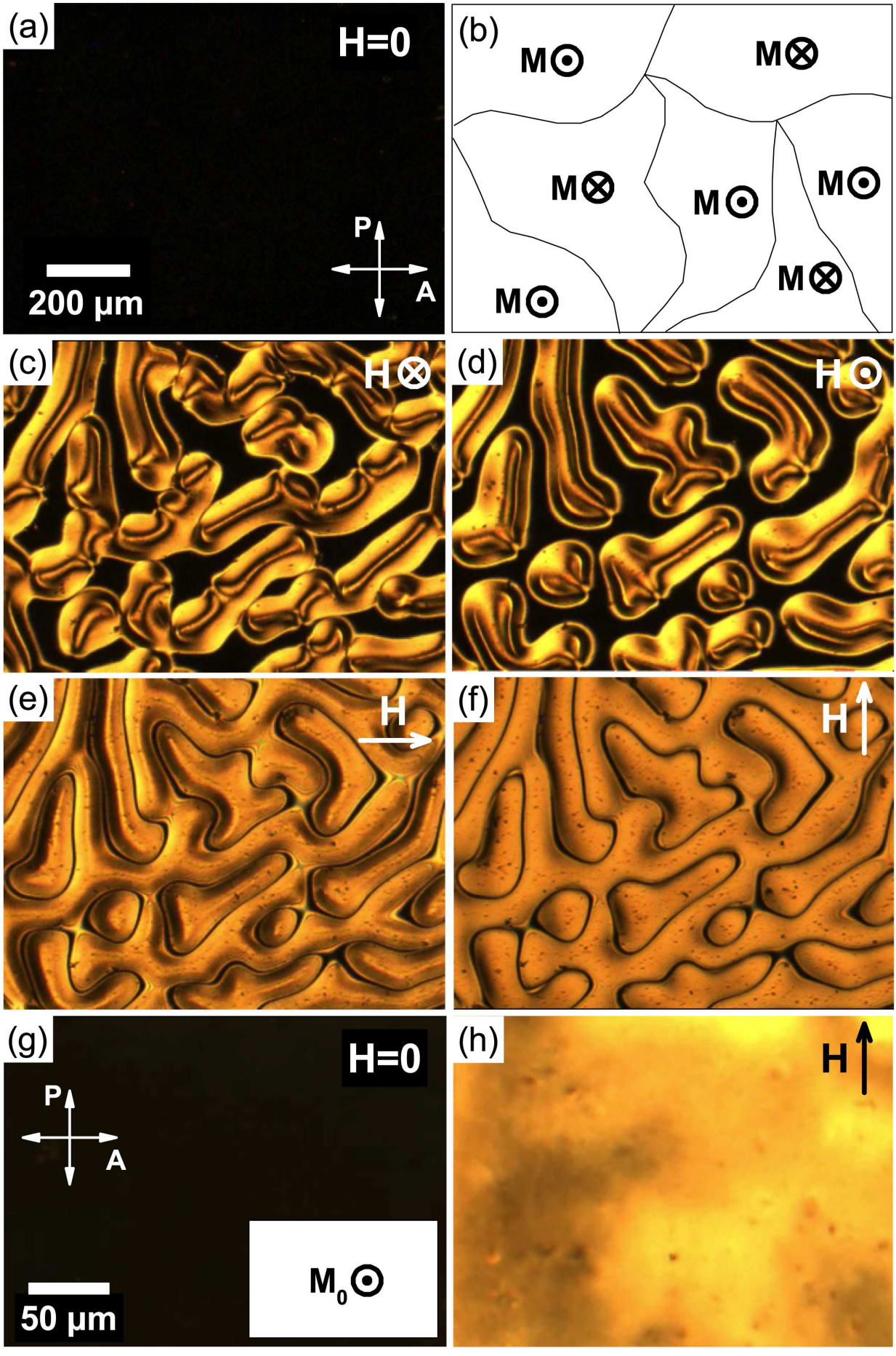

Figure 2 LE15437 04AUG2015

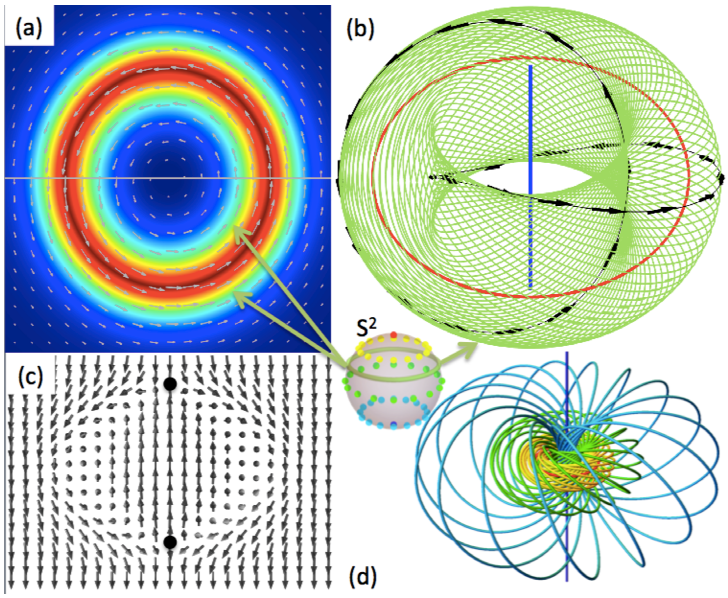

Figure 3 LE15437 04AUG2015

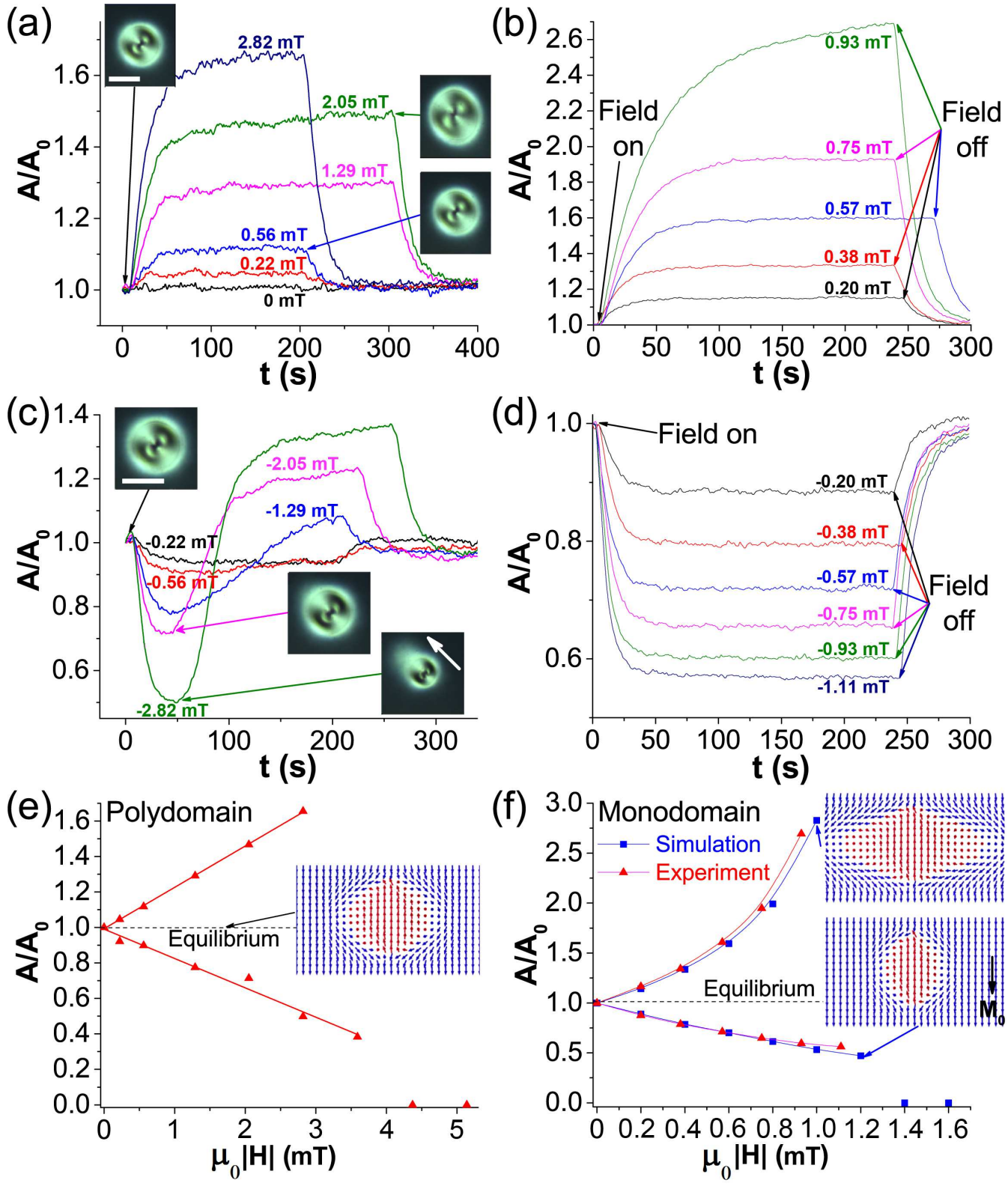

Figure 4 LE15437 04AUG2015

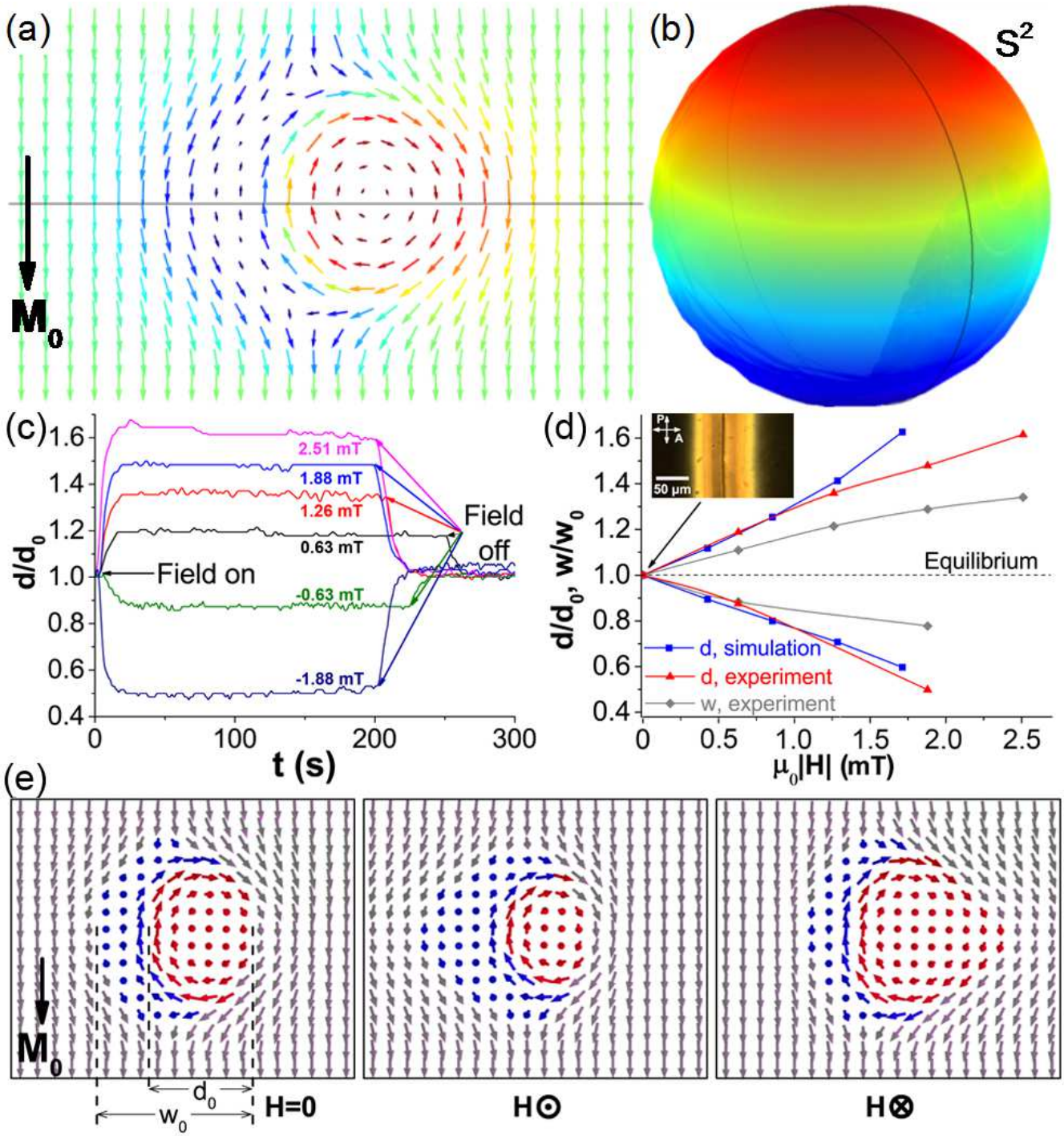

Figure 5 LE15437 04AUG2015